Rare Met. (2023) 42(5):1446–1452
https://doi.org/10.1007/s12598-022-02227-3

RARE METALS

LETTER

Spatially strain-induced and selective preparation of Mo_xN (x = 1, 2) as a highly effective nanoarchitectonic catalyst for hydrogen evolution reaction in a wide pH range

Chao Huang, Xiao-Lin Zhang, Jing Tang, Dan Li, Qing-Dong Ruan, Liang-Liang Liu, Fang-Yu Xiong, Bin Wang, Yue Xu, Sui-Han Cui, Yang Luo, Qing-Wei Li*, Paul K. Chu*

Received: 9 August 2022 / Revised: 14 September 2022 / Accepted: 30 September 2022 / Published online: 16 February 2023

Developing highly efficient catalysts for the hydrogen evolution reaction (HER) is crucial to commercial water splitting in the global efforts to mitigate fossil fuel combustion and combat global climate change. Molybdenum nitrides (Mo_xN) such as γ-Mo_2N and δ-MoN are promising HER catalysts. Although δ-MoN has better HER characteristics, controllable preparation of the materials is still challenging. Herein, selective preparation of γ-Mo_2N and δ-MoN is demonstrated by controlling the spatial stress. The hybrid δ-MoN and N-doped carbon composite (MoN/NC) consists of MoN layers and 1-nm-thick carbon layers. The carbon layers polarized by the high valence state of Mo in MoN provide the adsorption sites for H^+, and the NC layers also facilitate electron transport during the catalytic process. As a result, MoN/NC exhibits remarkable HER activity such as low overpotentials of 93, 211 and 141 mV to attain a current density of 10 $mA{\cdot}cm^{-2}$ as well as small Tafel slopes of 44.5, 83.2 and 65.4 $mV{\cdot}dec^{-1}$ in acidic, neutral and basic electrolytes of 0.5 $mol{\cdot}L^{-1}$ H_2SO_4, 1 $mol{\cdot}L^{-1}$ PBS, and 1 $mol{\cdot}L^{-1}$ KOH, respectively. The spatial stress effects enable selective preparation of specific phases in catalysts, and the pertinent mechanism provides important guidance to the preparation and optimization of advanced catalysts.

Hydrogen with a high energy density generated from renewable sources is one of the alternatives to fossil fuels, and water splitting is an attractive technique to mass produce hydrogen via the hydrogen evolution reaction (HER) [1]. Currently, noble-metal catalysts such as Pt show the highest activity, but the high cost and natural scarcity are limiting widespread adoption [2, 3]. Therefore, developing high-performance non-noble-metal catalysts is of paramount significance [4].

The cubic phase Mo_2N and hexagonal phase MoN are the two important structures of molybdenum nitride (Mo_xN) because of their similar electronic structures with Pt, good conductivity, and excellent corrosion resistance [5, 6]. Mo_2N is a promising electrode material for supercapacitors [7]. As for MoN, the superconductivity and layered structure make it more important in the catalysis

Supplementary Information The online version contains supplementary material available at https://doi.org/10.1007/s12598-022-02227-3.

C. Huang, X.-L. Zhang, J. Tang, D. Li, Q.-D. Ruan, L.-L. Liu, F.-Y. Xiong, B. Wang, Y. Xu, S.-H. Cui, Y. Luo, Q.-W. Li*, P. K. Chu*
Department of Physics, Department of Materials Science and Engineering, City University of Hong Kong, Hong Kong 999077, China
e-mail: qingweli@cityu.edu.hk

P. K. Chu
e-mail: paul.chu@cityu.edu.hk

C. Huang, X.-L. Zhang, J. Tang, D. Li, Q.-D. Ruan, L.-L. Liu, F.-Y. Xiong, B. Wang, Y. Xu, S.-H. Cui, Y. Luo, Q.-W. Li, P. K. Chu
Department of Biomedical Engineering, City University of Hong Kong, Hong Kong 999077, China

C. Huang
State Key Laboratory of Powder Metallurgy, Central South University, Changsha 410011, China

J. Tang
School of Mechanical Engineering, Liaoning Petrochemical University, Fushun 113001, China

Q.-W. Li
Advanced Research Institute for Multidisciplinary Science, Qilu University of Technology (Shandong Academy of Sciences), Jinan 250307, China

field [5, 8]. For example, Xie et al. [5] have synthesized ultrathin MoN nanosheets with exposed Mo active sites showing good HER characteristics in an acid medium. Generally, fabrication of Mo_xN requires a high temperature higher than 800 °C, which may cause particle aggregation and sintering [8]. In addition, the catalytic performance and long-term stability of γ-Mo_2N are lower than those of δ-MoN as demonstrated by Zou et al. [9] and Hu et al. [6] Direct nitridation of MoO_3 at 800 °C produces crystalline γ-Mo_2N [7]. Finding a new strategy to convert Mo_2N to MoN would promote HER performance greatly. For example, Xiong et al. [10] have prepared two-dimensional defect-rich MoN nanosheets by a NaCl template-directed synthesis technique, and the materials show a small overpotential of 125 mV at a current density of 10 $mA{\cdot}cm^{-2}$ in 0.5 $mol{\cdot}L^{-1}$ H_2SO_4. Song et al. [8] have prepared MoN nano-hexagonal prisms with a specific precursor such as hexagonal MoO_3 (h-MoO_3) in lieu of common orthorhombic MoO_3 (α-MoO_3). All in all, in spite of recent advance, it is still challenging to fabricate δ-MoN using α-MoO_3 as precursor.

Herein, selective synthesis of γ-Mo_2N and δ-MoN is demonstrated by exploiting the spatial strain effect. Nitridation of MoO_3 at 800 °C produces crystalline γ-Mo_2N. An atomic interlayer of MoO_3 is inserted with dodecylamine (DDA) molecules (MoO_3/DDA), and during nitridation at 800 °C, the hybrid δ-MoN and N-doped carbon (MoN/NC) is prepared. The synthesis process is universal in nature, and the DDA layer plays a crucial role in the formation of δ-MoN. The MoO_3 layers are separated and stabilized between the DDA layers, thus inhibiting restacking and aggregation of MoO_3 in the vertical direction. Based on the spatial strain effect, MoO_3 is converted in situ into δ-MoN, and the carbon layers are polarized due to the high valence state of Mo in MoN and then supply the actual active sites for HER. The NC layers also facilitate electron transport during the catalytic process. Consequently, MoN/NC exhibits remarkable HER activity as exampled by low overpotentials of 93, 211 and 141 mV to reach a current density of 10 $mA{\cdot}cm^{-2}$ as well as small Tafel slopes of 44.5, 83.2 and 65.4 $mV{\cdot}dec^{-1}$ in 0.5 $mol{\cdot}L^{-1}$ H_2SO_4, 1 $mol{\cdot}L^{-1}$ PBS, 1 $mol{\cdot}L^{-1}$ KOH,

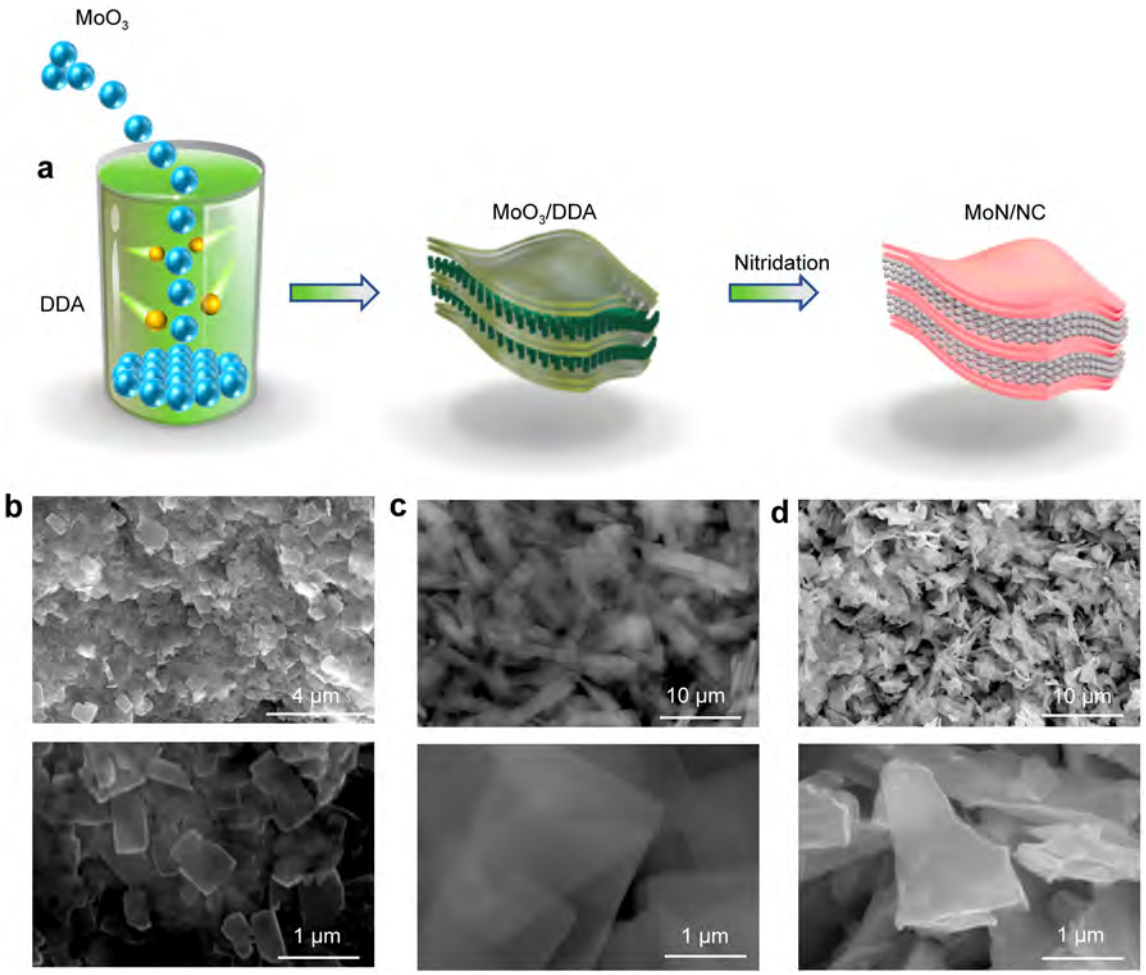

Fig. 1 **a** Synthesis of MoN/NC; **b** SEM images of MoO_3; **c** SEM images of MoO_3/DDA; **d** SEM images of MoN/NC

respectively, verifying the adaptability to a wide pH range. The spatial stress strategy provides insights into selective preparation of specific phases in catalysts boding well for optimization of advanced catalysts.

Figure 1a shows the schematic diagram of the selective synthesis of δ-MoN/NC. The MoO_3 precursor has a layered structure along the [0*b*0] direction with an interlayer spacing d_{010} of 0.69 nm (Fig. S1a) [11–13]. δ-MoN has the typical hexagonal crystal structure with a layered configuration containing exposed Mo sites (Fig. S1b), whereas γ-Mo_2N has a cubic structure without exposed Mo active sites (Fig. S1c). X-ray diffraction (XRD) pattern of MoO_3 reveals the three typical peaks of (020), (040), (060) at 12.7°, 25.7°, 38.9°, respectively (Fig. S2a), indicative of the layered structure. The scanning electron microscopy (SEM) images show that the precursor has a nanosheet morphology (Fig. S2b, c). The pristine MoO_3 nanosheets are nitridated at 800 °C to produce single-crystal γ-Mo_2N (JCPDS No. 25-1366) (Fig. S3), and the nanosheet structure shows some aggregation [14]. Since MoO_3 has a layered structure, the dodecylamine (DDA) molecules can be inserted easily into the interlayered space of MoO_3 along the *b* direction (MoO_3/DDA) by electrostatic attraction (Fig. S4) [15]. The molar ratios of MoO_3 and DDA are presented in Fig. S5. With increased DDA concentrations, the morphology of MoO_3/DDA changes from disorganized to orderly and disorganized again. Hence, a molar ratio of 1: 3 (MoO_3 to DDA) is determined to be the best. After nitridation of MoO_3/DDA at 800 °C, hybrid MoN and N-doped carbon (MoN/NC) is prepared by converting MoO_3 into MoN and DDA into NC (Fig. 1a). Compared to the nanosheet morphology of pure MoO_3 (Fig. 1b), MoO_3/DDA has a translucent structure indicating that the nanosheets are quite thin (Fig. 1c).

Fourier transform infrared spectroscopy (FTIR) demonstrates that aniline species are inserted into the interlayer of MoO_3 as shown in Fig. S6. The MoO_3 nanosheets display four typical peaks, including the Mo–O vibrational peaks at 452 and 521 cm^{-1} and Mo=O stretching peaks at 821 and 993 cm^{-1} [16]. After insertion with aniline, the Mo–O peak at 452 cm^{-1} sharpens and a new peak at 853 cm^{-1} corresponds to Mo–O–Mo stretching, implying that the vibrational mode of Mo–O changes due to extrusion by adjacent aniline molecules [12]. Furthermore, new peaks at 1,260, 1,390, 1,500 and 1,644 cm^{-1} associated with C–N stretching, C−H bending, N–H stretching, and C–C stretching are observed, respectively, further corroborating that DDA species are inserted into the interlayer of MoO_3. In the subsequent nitridation process, DDA layer plays a crucial role in the formation of δ-MoN. The MoO_3 layers are separated and stabilized between the DDA layers, hindering restacking and aggregation of MoO_3 in the vertical direction. By taking advantage of the spatial strain effect, MoO_3 is converted in situ into δ-MoN. The MoN/NC surface (Fig. 1d) becomes uneven because the structure shrinks from MoO_3 to MoN.

Figure 2a depicts XRD patterns of MoN/NC and Mo_2N. After nitridation at 800 °C, MoO_3/DDA is converted into MoN/NC rather than Mo_2N/NC due to the spatial strain effect arising from DDA [17]. X-ray photoelectron spectroscopy (XPS) spectra of MoN/NC and Mo_2N/NC in Fig. S7 show that the products contain Mo, N, O, and C. There are three pairs of peaks in the XPS Mo 3d spectra. The peaks at 235.7/232.5 eV are related to the Mo^{3+} state in Mo–N, whereas the peaks at 232.9/229.75 eV and 231.9/229.2 eV are attributed to Mo^{4+} and Mo^{6+} of Mo–O, respectively [18]. According to previous reports, formation of Mo^{4+} and Mo^{6+} stems from partial surface oxidation of Mo_2N or MoN in air [19]. The Mo–N bond in MoN is stronger, and therefore, the NC layers can better resist oxidation of MoN than that in Mo_2N. The N 1s XPS spectra of MoN/NC can be deconvoluted into three peaks at 395.5 eV for Mo $2p_{3/2}$, 397.7 eV for N–Mo, and 401.5 eV for N–C, indicating that the N is incorporated into the carbon layer [20, 21]. The high-resolution TEM (HRTEM) images in Fig. 2d–f disclose the structure of MoN/NC. As shown in Fig. 2e, MoN shows an atomic arrangement in which the lattices are aligned in the same direction. The large interlayer spacing of 1.04 nm corresponds to the carbon layer from DDA. The magnified TEM image (Fig. 2f) clearly shows the lattice fringe of 0.25 nm stemming from the (200) plane of MoN [6]. The energy-dispersive X-ray spectroscopy (EDS) elemental maps confirm uniform distributions of Mo, N, and C in the nanosheets. These results indicate that the sandwiched structure of MoN/NC is prepared by exploiting the spatial strain effect of NC. The HER activities of MoN/NC, Mo_2N, NC are evaluated by linear sweep voltammetry (LSV) in 0.5 mol·L^{-1} H_2SO_4, 1 mol·L^{-1} PBS, and 1 mol·L^{-1} KOH to investigate the performance in different pH values. The polarization curves are *iR* corrected. Considering the unique structure of MoN/NC and conductive NC layer, good HER characteristics are expected from MoN/NC. As confirmed by Fig. 3a–c, MoN/NC indeed shows remarkable HER activities such as low overpotentials of 93, 211 and 141 mV to attain a current density of 10 mA·cm^{-2} in 0.5 mol·L^{-1} H_2SO_4, 1 mol·L^{-1} PBS, and 1 mol·L^{-1} KOH, respectively, and it is noted that the performance is similar to that of Pt/C. The HER characteristics of MoN/NC are better than those of other recently reported MoN-based catalysts such as MoS_2-Mo_2N/CC, Dr-MoN-0, C_3N_4/MoN mixture, MoN_x and MoS_2/MoN (Table S1). As shown in Fig. 3d–f, MoN/NC shows small Tafel slopes of 44.5, 83.2 and 65.4 mV·dec^{-1} in 0.5 mol·L^{-1} H_2SO_4, 1 mol·L^{-1} PBS, and 1 mol·L^{-1} KOH,

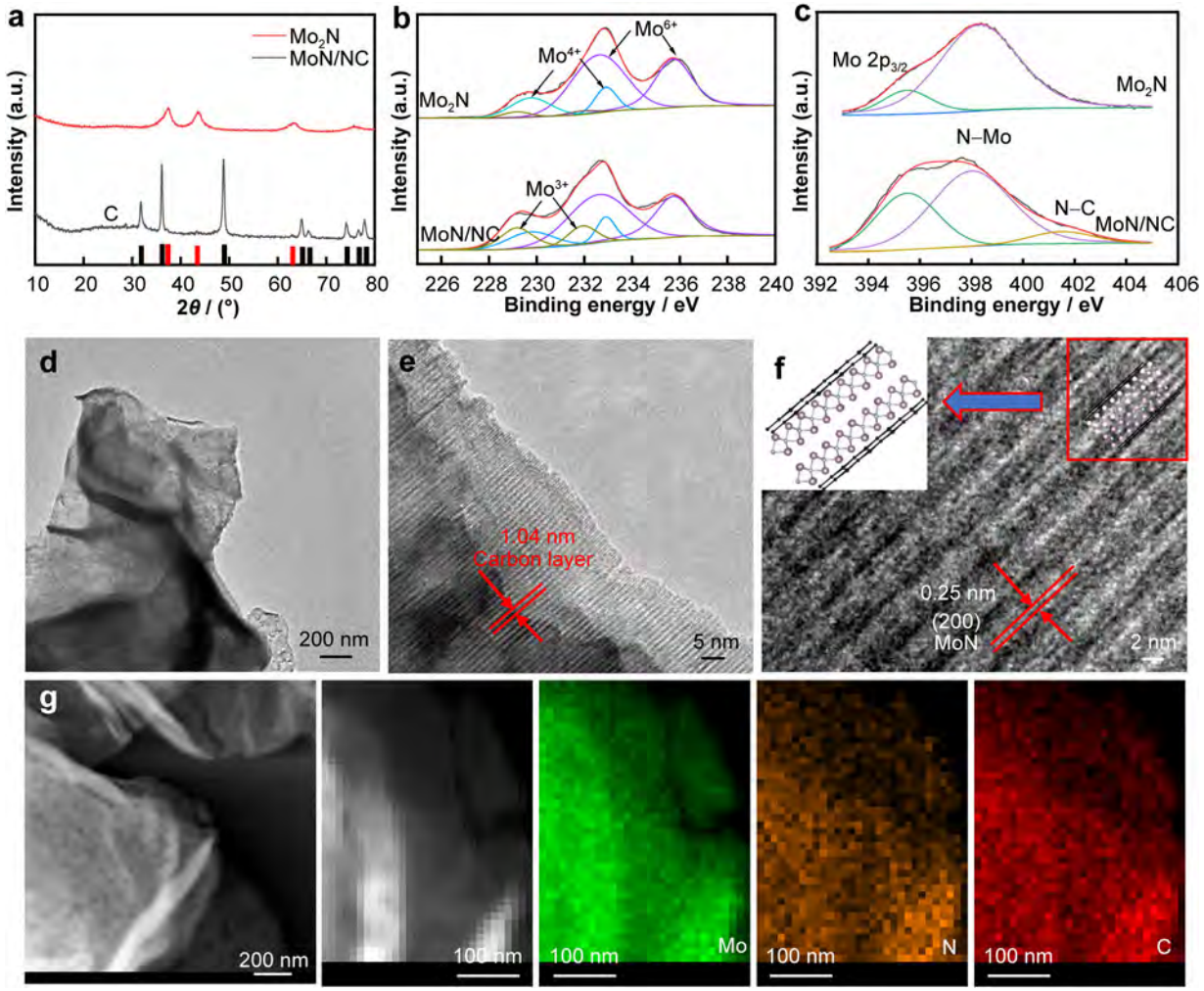

Fig. 2 **a** XRD patterns of MoN/NC and Mo_2N; **b** Mo 3d XPS spectra of MoN/NC and Mo_2N; **c** N 1s XPS spectra of MoN/NC and Mo_2N; **d–f** TEM images of MoN/NC and (inset) lattice fringe image of MoN/NC; **g** elemental maps of MoN/NC

respectively, which are in fact lower than those of Mo_2N, thereby corroborating the good HER kinetics [22].

To explore the intrinsic activity, the electrochemical surface area (ECSA) is calculated based on the electrochemical double-layer capacitance (C_{dl}) in the non-Faradic region of the CV curves (Fig. S8) [23, 24]. C_{dl} is determined according to the current density versus scanning rate relationship shown in Fig. 3g–i. Although Mo_2N has a larger ECSA, the intrinsic activity of Mo_2N is lower than that of MoN/NC in 0.5 mol·L^{-1} H_2SO_4, 1 mol·L^{-1} PBS, and 1 mol·L^{-1} KOH (Fig. S9). To determine the charge transferability, the electrochemical impedance spectra (EIS) are acquired. MoN/NC shows lower resistances of 21, 174 and 104 Ω in 0.5 mol·L^{-1} H_2SO_4, 1 mol·L^{-1} PBS, and 1 mol·L^{-1} KOH, respectively, than Mo_2N (Fig. S10).

To analyze the roles of the intermediate species and actual active sites in HER, in situ Raman scattering is performed at an applied potential of 0.1 V [25, 26]. As shown in Fig. 4a, no MoN peaks are observed and the two carbon peaks at 1,370 and 1,590 cm^{-1} are the D and G bands of NC, respectively, indicating that the MoN surface is covered by a thin carbon layer [27, 28]. As the overpotential goes up, the D and G bands of pure NC show no obvious change (Fig. 4b), indicative of the weak catalytic effects of NC. However, as shown in Raman scattering spectrum of MoN/NC, the G bond becomes sharper because the adsorption of H on the C site changes the vibrational modes of carbon, and consequently, polarization of carbon produces the H^+ adsorbed sites in HER [29]. Furthermore, a stable current showing a decrease of less than 3% is observed in the continuous 70 *i-t* test at the fixed overpotential of − 0.1 V (vs. RHE) (Fig. S11). XRD pattern acquired after the test shows weak H_2MoO_4 peaks (Fig. S12), implying that some MoN is converted to H_2MoO_4 at the catalyst surface [30]. The results corroborate the synergistic effects rendered by the MoN and NC layers.

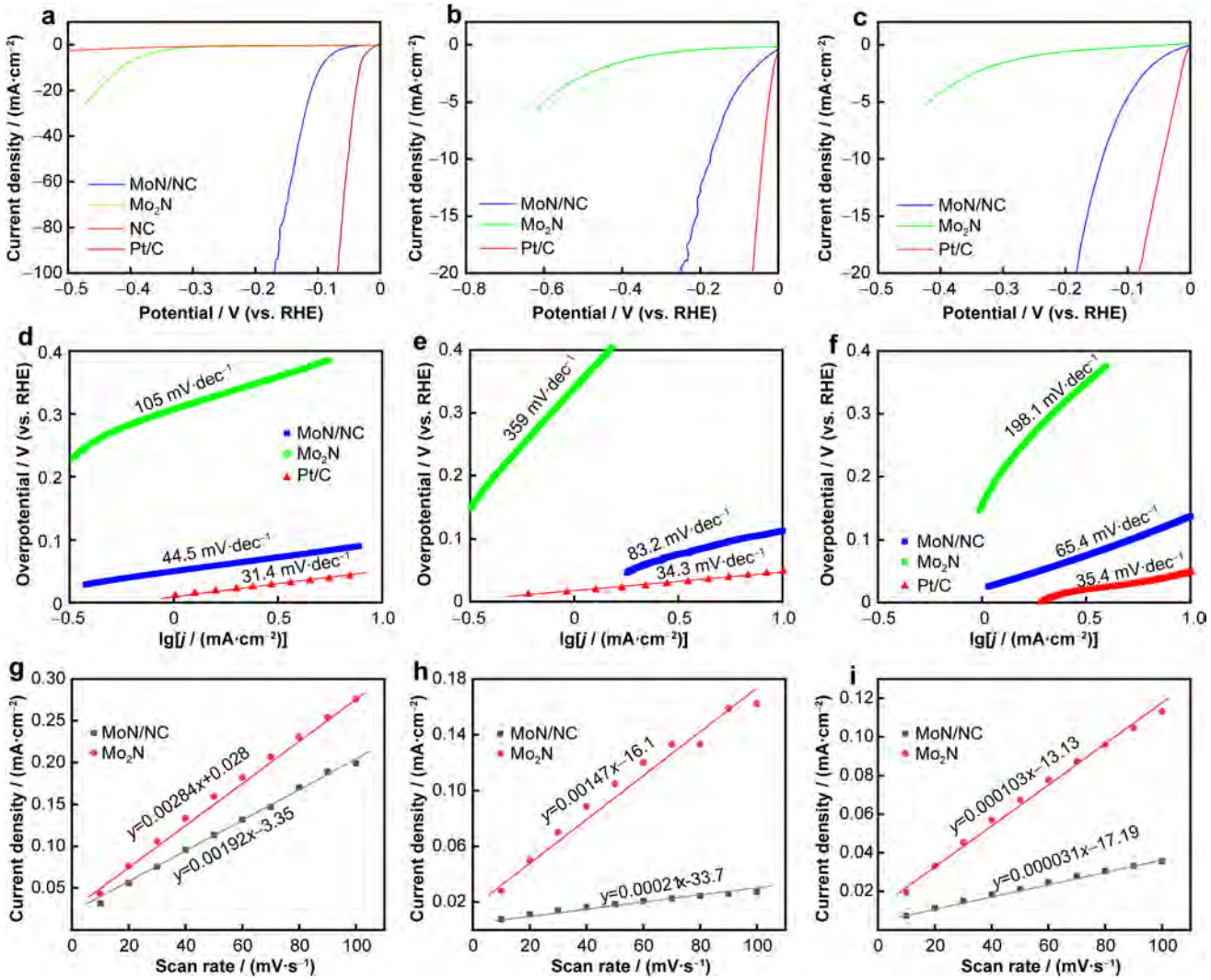

Fig. 3 **a–c** LSV curves of MoN/NC, Mo_2N, Pt/C in 0.5 mol·L^{-1} H_2SO_4, 1 mol·L^{-1} PBS, and 1 mol·L^{-1} KOH, respectively; **d–f** Tafel slopes of MoN/NC, Mo_2N, Pt/C in 0.5 mol·L^{-1} H_2SO_4, 1 mol·L^{-1} PBS, and 1 mol·L^{-1} KOH, respectively; **g–i** C_{dl} curves of MoN/NC, Mo_2N in 0.5 mol·L^{-1} H_2SO_4, 1 mol·L^{-1} PBS, and 1 mol·L^{-1} KOH, respectively

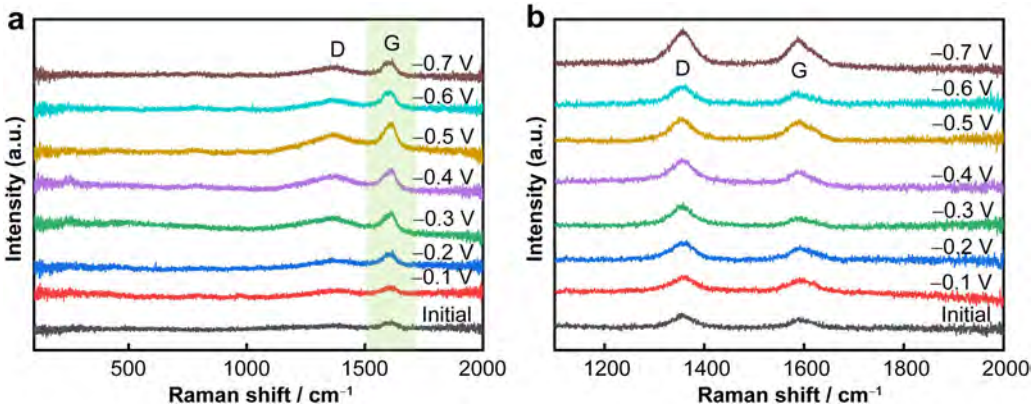

Fig. 4 **a** In situ Raman scattering spectra of MoN/NC and **b** in situ Raman scattering spectra of NC

In summary, selective preparation of δ-MoN and γ-Mo_2N is demonstrated by controlling the spatial stress. The hybrid δ-MoN and N-doped carbon (MoN/NC) consists of MoN layers and 1-nm thick carbon layers. The carbon layers polarized by the high valence state of Mo in MoN provide the adsorption sites for H^+, and the NC layers facilitate electron transport while providing good structural and electrochemical durability. As a consequence, MoN/NC delivers remarkable HER performance as exemplified by low overpotentials of 93, 211 and 141 mV for a current density of 10 mA·cm^{-2} besides small Tafel slopes of 44.5, 83.2 and 65.4 mV·dec^{-1} in 0.5 mol·L^{-1} H_2SO_4, 1 mol·L^{-1} PBS, and 1 mol·L^{-1} KOH, respectively. The results confirm the high activity in a wide pH range. The spatial stress strategy and knowledge of the mechanism not only broaden our understanding of selective preparation and specific exposure of active atoms, but also provide insights into how to prepare and optimize advanced catalysts.

Acknowledgments This study was financially supported by Hong Kong Scholars Program (No. XJ2018009), City University of Hong Kong Strategic Research Grant (SRG) (No. 7005505), City University of Hong Kong Donation Research Grant (No. 9229021), the National Natural Science Foundation of China (No. 52003129), Shandong Provincial Natural Science Foundation, China (No. ZR2019BB006) and State Key Laboratory of Powder Metallurgy, Central South University, Changsha, China.

Declarations

Conflict of interests The authors declare that they have no conflict of interest.

References

[1] Shi Y, Zhang B. Recent advances in transition metal phosphide nanomaterials: synthesis and applications in hydrogen evolution reaction. Chem Soc Rev. 2016;45(6):1529. https://doi.org/10.1039/C5CS00434A.

[2] Huang C, Wu D, Qin P, Ding K, Pi C, Ruan Q, Song H, Gao B, Chen H, Chu PK. Ultrafine Co nanodots embedded in N-doped carbon nanotubes grafted on hexagonal VN for highly efficient overall water splitting. Nano Energy. 2020;73:104788. https://doi.org/10.1016/j.nanoen.2020.104788.

[3] Huang C, Miao X, Pi C, Gao B, Zhang X, Qin P, Huo K, Peng X, Chu PK. Mo_2C/VC heterojunction embedded in graphitic carbon network: an advanced electrocatalyst for hydrogen evolution. Nano Energy. 2019;60:520. https://doi.org/10.1016/j.nanoen.2019.03.088.

[4] Huang C, Qin P, Luo Y, Ruan QD, Liu LL, Wu YZ, Li QW, Xu Y, Liu RG, Chu PK. Recent progress and perspective of cobalt-based catalysts for water splitting: design and nanoarchitectonics. Materials Today Energy. 2022;23:100911. https://doi.org/10.1016/j.mtener.2021.100911.

[5] Xie JF, Li S, Zhang XD, Zhang JJ, Wang RX, Zhang H, Pan BC, Xie Y. Atomically-thin molybdenum nitride nanosheets with exposed active surface sites for efficient hydrogen evolution. Chem Sci. 2014;5(12):4615. https://doi.org/10.1039/C4SC02019G.

[6] Sun JW, Xu WJ, Lv CX, Zhang LJ, Shakouri MS, Peng YH, Wang QQ, Yang XF, Yuan D, Huang MH, Hu YF, Yang DJ, Zhang LX. Co/MoN hetero-interface nanoflake array with enhanced water dissociation capability achieves the Pt-like hydrogen evolution catalytic performance. Appl Catal B-Environ. 2021;286:119882. https://doi.org/10.1016/j.apcatb.2021.119882.

[7] Ma GQ, Wang Z, Gao B, Ding TP, Zhong QZ, Peng X, Su J, Hu B, Yuan LY, Chu PK, Zhou J, Huo KF. Multilayered paper-like electrodes composed of alternating stacked mesoporous Mo_2N nanobelts and reduced graphene oxide for flexible all-solid-state supercapacitors. J Mater Chem A. 2015;3(28):14617. https://doi.org/10.1039/C5TA02851E.

[8] Song XY, Yi WC, Li JF, Kong QH, Bai H, Xi GC. Selective preparation of Mo_2N and MoN with high surface area for flexible SERS sensing. Nano Lett. 2021;21(10):4410. https://doi.org/10.1021/acs.nanolett.1c01099.

[9] Lang X, Qadeer MA, Shen G, Zhang R, Yang S, An J, Pan L, Zou JJ. A Co–Mo_2N composite on a nitrogen-doped carbon matrix with hydrogen evolution activity comparable to that of Pt/C in alkaline media. J Mater Chem A. 2019;7(36):20579. https://doi.org/10.1039/C9TA07749A.

[10] Xiong J, Cai WW, Shi WJ, Zhang XL, Li J, Yang ZH, Feng LG, Cheng HS. Salt-templated synthesis of defect-rich MoN nanosheets for boosted hydrogen evolution reaction. J Mater Chem A. 2017;5(46):24193. https://doi.org/10.1039/C7TA07566A.

[11] Liao ZH, Li QW, Zhang JB, Xu J, Gao BA, Chu PK, Huo KF. Oriented MoS_2 nanoflakes on N-doped carbon nanosheets derived from dodecylamine-intercalated MoO_3 for high-performance lithium-ion battery anodes. Chem Electro Chem. 2018;5(10):1350. https://doi.org/10.1002/celc.201800092.

[12] Huang C, Pi C, Zhang X, Ding K, Qin P, Fu J, Peng X, Gao B, Chu PK, Huo K. In situ synthesis of MoP nanoflakes intercalated N-doped graphene nanobelts from MoO_3–amine hybrid for high-efficient hydrogen evolution reaction. Small. 2018;14(25):1800667. https://doi.org/10.1002/smll.201800667.

[13] Qin P, Zhang S-Q, Huang Z-F, Gao B. Disclosure of charge storage mechanisms in molybdenum oxide nanobelts with enhanced supercapacitive performance induced by oxygen deficiency. Rare Met. 2021;40(9):2447. https://doi.org/10.1007/s12598-021-01722-3.

[14] Liu JB, Gong HS, Ye GL, Fei HL. Graphene oxide-derived single-atom catalysts for electrochemical energy conversion. Rare Met. 2022;41(5):1703. https://doi.org/10.1007/s12598-021-01904-z.

[15] Ji HM, Liu XL, Liu ZJ, Yan B, Chen L, Xie YF, Liu C, Hou WH, Yang G. In situ preparation of sandwich MoO_3/C hybrid nanostructures for high-rate and ultralong-life supercapacitors. Adv Func Mater. 2015;25(12):1886. https://doi.org/10.1002/adfm.201404378.

[16] Sen SK, Dutta S, Khan MR, Manir MS, Dutta S, Al MA, Razia S, Hakim MA. Characterization and antibacterial activity study of hydrothermally synthesized h-MoO_3 nanorods and alpha--MoO_3 nanoplates. Bionanoscience. 2019;9(4):87382. https://doi.org/10.1007/s12668-019-00671-7.

[17] Kang WJ, Feng Y, Li Z, Yang WQ, Cheng CQ, Shi ZZ, Yin PF, Shen GR, Yang J, Dong CK, Liu H, Ye FX, Du XW. Strain-activated copper catalyst for pH-universal hydrogen evolution reaction. Adv Func Mater. 2022;32(18):2112367. https://doi.org/10.1002/adfm.202112367.

[18] Sun JH, Guo FF, Li XY, Yang J, Ma JF. Constructing Ni/MoN heterostructure nanorod arrays anchored on Ni foam for efficient hydrogen evolution reaction under alkaline conditions. Sustain Energy Fuels. 2021;5(21):5565. https://doi.org/10.1039/D1SE01283E.

[19] Wang Y, Sun Y, Yan F, Zhu CL, Gao P, Zhang XT, Chen YJ. Self-supported NiMo-based nanowire arrays as bifunctional electrocatalysts for full water splitting. J Mater Chem A. 2018; 6(18):8479. https://doi.org/10.1039/C8TA00517F.

[20] Guo ZY, Zhong Y, Xuan ZW, Mao CM, Du FL, Li GC. Polypyrrole-assisted synthesis of roselike MoS_2/nitrogen-containing carbon/graphene hybrids and their robust lithium storage performances. RSC Adv. 2015;5(77):62624. https://doi.org/10.1039/C5RA09092J.

[21] Wang ML, Cui MZ, Liu WF, Liu XG, Xu BS. Facile synthesis of cyclodextrin functionalized reduced graphite oxide with the aid of ionic liquid for simultaneous determination of guanine and adenine. Electroanalysis. 2018;30(5):842. https://doi.org/10.1002/elan.201700715.

[22] Xiang R, Duan YJ, Peng LS, Wang Y, Tong C, Zhang L, Wei ZD. Three-dimensional Core@Shell Co@$CoMoO_4$ nanowire arrays as efficient alkaline hydrogen evolution electro-catalysts. Appl Catal B-Environ. 2019;246:41. https://doi.org/10.1016/j.apcatb.2019.01.035.

[23] Yu L, Mishra IK, Xie Y, Zhou H, Sun J, Zhou J, Ni Y, Luo D, Yu F, Yu Y. Ternary $Ni_{2(1-x)}Mo_{2x}P$ nanowire arrays toward efficient and stable hydrogen evolution electrocatalysis under large-current-density. Nano Energy. 2018;53:492. https://doi.org/10.1016/j.nanoen.2018.08.025.

[24] Hui L, Xue Y, Huang B, Yu H, Zhang C, Zhang D, Jia D, Zhao Y, Li Y, Liu H. Overall water splitting by graphdiyne-exfoliated and-sandwiched layered double-hydroxide nanosheet arrays. Nat Commun. 2018;9(1):1. https://doi.org/10.1038/s41467-018-07790-x.

[25] Huang C, Chu PK. Recommended practices and benchmarking of foam electrodes in water splitting. Trends Chem. 2022;4(25): 1065. https://doi.org/10.1016/j.trechm.2022.09.008.

[26] Huang C, Zhang B, Wu Y, Ruan Q, Liu L, Su J, Tang Y, Liu R, Chu PK. Experimental and theoretical investigation of reconstruction and active phases on honeycombed Ni_3N-Co_3N/C in water splitting. Appl Catal B. 2021;297:120461. https://doi.org/10.1016/j.apcatb.2021.120461.

[27] Sun C, Zhao YJ, Yuan XY, Li JB, Jin HB. Bimetal nanoparticles hybridized with carbon nanotube boosting bifunctional oxygen electrocatalytic performance. Rare Met. 2022;41(8):2616. https://doi.org/10.1007/s12598-022-02021-1.

[28] Cai HZ, Yi JH, Wu F, Wei Y, Zhang XX, Hu CY. Preparation and characterization of tantalum coating on porous carbon foam by chemical vapor deposition. Chin J Rare Metals. 2020;44(10): 1108. https://doi.org/10.13373/j.cnki.cjrm.XY19040006

[29] Vecera P, Chacon-Torres JC, Pichler T, Reich S, Soni HR, Gorling A, Edelthalhammer K, Peterlik H, Hauke F, Hirsch A. Precise determination of graphene functionalization by in situ raman spectroscopy. Nat Commun. 2017;8:15192. https://doi.org/10.1038/s41467-022-34281-x.

[30] Cui JX, Wang WS, Zhen L, Shao WZ, Chen ZL. Formation of $FeMoO_4$ hollow microspheres via a chemical conversion-induced ostwald ripening process. Cryst Eng Comm. 2012;14(20): 7025. https://doi.org/10.1039/C2CE25825K.

Springer

RARE METALS

Supporting Information

Spatially strain-induced and selective preparation of Mo_xN (x = 1, 2) as a highly effective nanoarchitectonic catalyst for the hydrogen evolution reaction in a wide pH range

Chao Huang, Xiao-Lin Zhang, Jing Tang, Dan Li, Qing-Dong Ruan, Liang-Liang Liu, Fang-Yu Xiong, Bin Wang, Yue Xu, Sui-Han Cui, Yang Luo, Qing-Wei Li,* and Paul K. Chu*

C. Huang, X.-L. Zhang, D. Li, Q.-D. Ruan, L.-L. Liu, F.-Y. Xiong, B.Wang, Y. Xu, S.-H. Cui, Y. Luo, Q.-W. Li*, P.-K. Chu*
Department of Physics, Department of Materials Science and Engineering, and Department of Biomedical Engineering, City University of Hong Kong, Tat Chee Avenue, Kowloon, Hong Kong, China
e-mail: paul.chu@cityu.edu.hk of P.-K. Chu

C. Huang
State Key Laboratory of Powder Metallurgy, Central South University, Changsha, China

J. Tang
School of Mechanical Engineering, Liaoning Petrochemical University, No. 1, Dandong Road, Fushun 113001, Liaoning, China

Q.-W. Li
Advanced Research Institute for Multidisciplinary Science, Qilu University of Technology (Shandong Academy of Sciences), Daxue Road 3501, Jinan 250307, Shandong Province, China
e-mail: qingweli@cityu.edu.hk of Q.-W. Li

2. Experimental methods

2.1 Materials preparation

All the chemicals were purchased from Sigma. Dodecylamine (DDA) (1.5 g) was dissolved into 58 mL of ethanol and α-MoO_3 (0,5 g) was added and kept at 70 ºC for 24 h.[1, 2] After cooling to room temperature, the samples were washed with ethanol and dried at 60 ºC overnight. The as-prepared precursor was heated to 800 ºC under flowing NH_3 to prepare the hybrid MoN and N-doped carbon (NC) (MoN/NC) products. For comparison, Mo_2N was prepared by direct nitridation of α-MoO_3 at 800 ºC without DDA.

2.2 Materials Characterization

The phase and morphology of the samples were characterized by X-ray diffraction (XRD, Bruker AXS D2 Phaser) using Cu K_α radiation (λ = 1.5418Å), field-emission scanning electron microscopy (FE-SEM, Thermo Fisher QUATTRO S), and transmission electron microscopy (HR-TEM, FEI Titan G2 60-300), respectively. The elemental analysis was performed by X-ray photoelectron spectroscopy (XPS, ESCALB MK-II, VG Instruments, UK) and *in situ* Raman scattering was conducted on the LabRAM HR800 laser confocal micro-Raman spectrometer using a laser wavelength of 514.5 nm.

2.3 Electrochemical Measurements

The electrochemical measurements were conducted in a three-electrode cell in an electrochemical workstation (CHI660d) at 25 ºC in H_2-saturated 0.5 M H_2SO_4, 1 M PBS, and 1 M KOH. The working electrode was prepared with 5 uL of the electrocatalytic solution loaded onto the glass carbon electrode (GCE) surface and covered with a thin Nafion layer. The electrocatalytic solution contained 24 mg of the sample and 6 mL of deionized water. The loading density of the catalyst on GCE was calculated to 0.28 mg cm^{-2}. The scanning

voltammetry curves were acquired in H_2-saturated 0.5 M H_2SO_4, 1 M PBS, and 1 M KOH at a scanning rate of 5 mV s^{-1}. The electrochemically active surface areas (ECSA) and electrochemical double layer capacitances (Cdl) were determined on the CHI660b at different scanning rates from 10 mV s^{-1} to 100 mV s^{-1}. Electrochemical impedance spectroscopy (EIS) was carried out at an overpotential of 100 mV and frequencies between 100 kHz and 0.1 Hz. All the potentials were converted to the RHE scale by calibration ($E_{RHE} = E_{SCE} + 0.059pH + 0.241$) and *iR* corrected using *Rs* obtained by EIS.

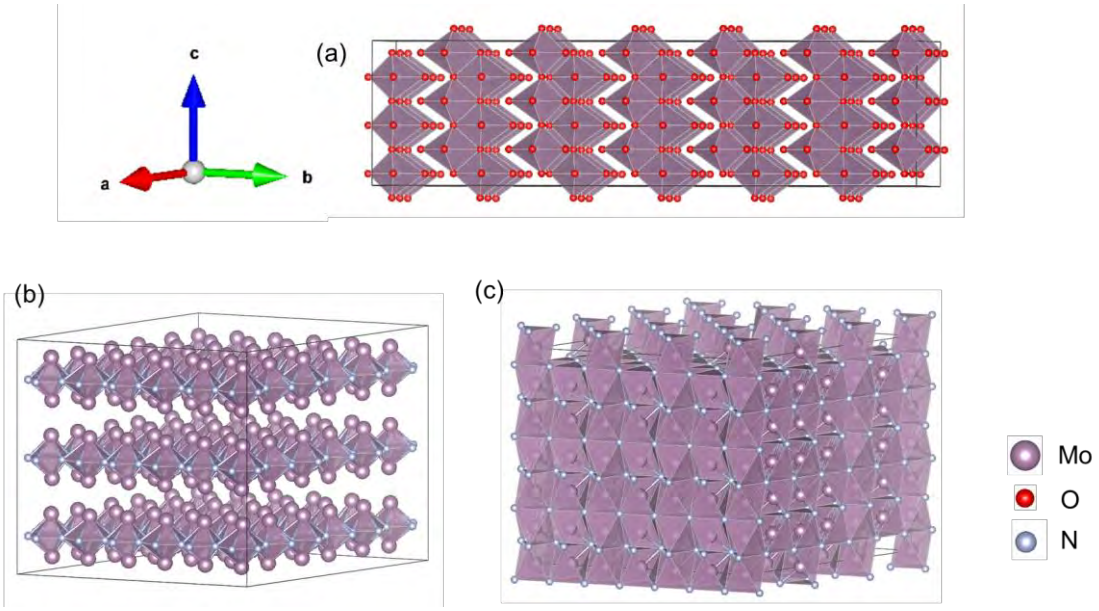

Figure S1. (a) Crystal structure of MoO_3, (b) Crystal structure of MoN, and (c) crystal structure of Mo_2N.

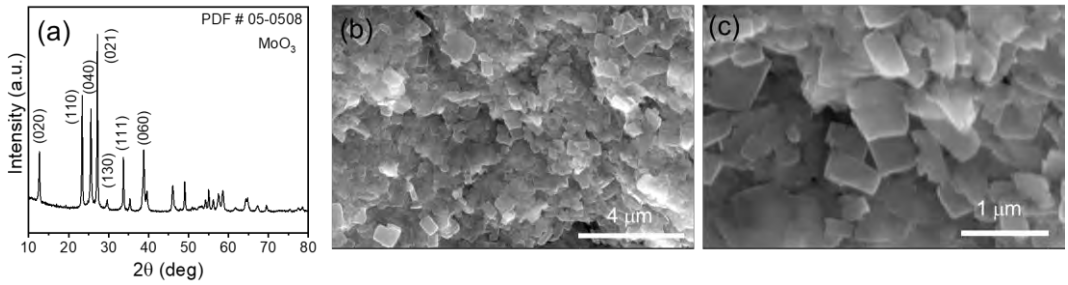

Figure S2. (a) XRD spectrum of MoO_3 and (b, c) SEM images of MoO_3.

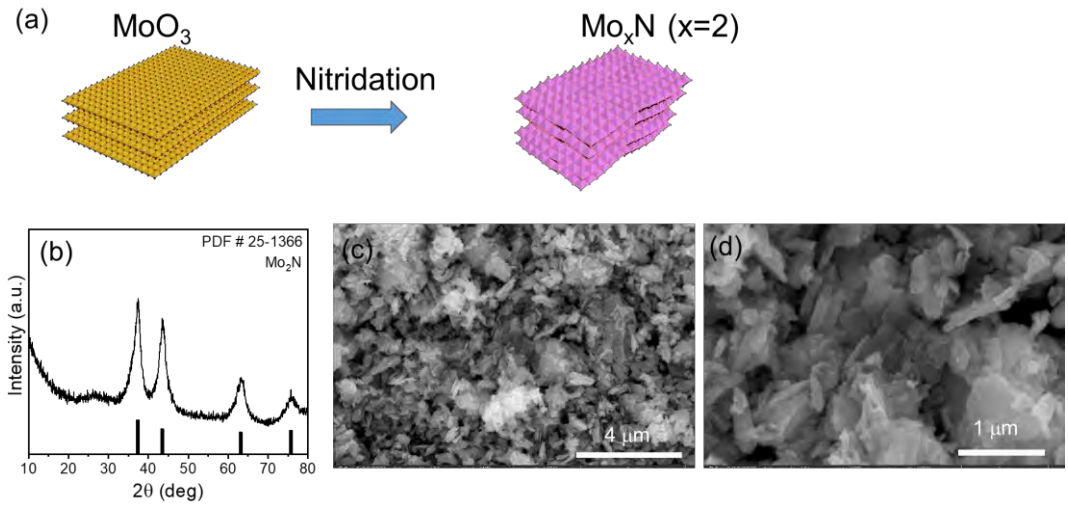

Figure S3. (a) Synthesis of Mo_2N; (b) XRD spectrum of Mo_2N; (c) and (d) SEM images of Mo_2N.

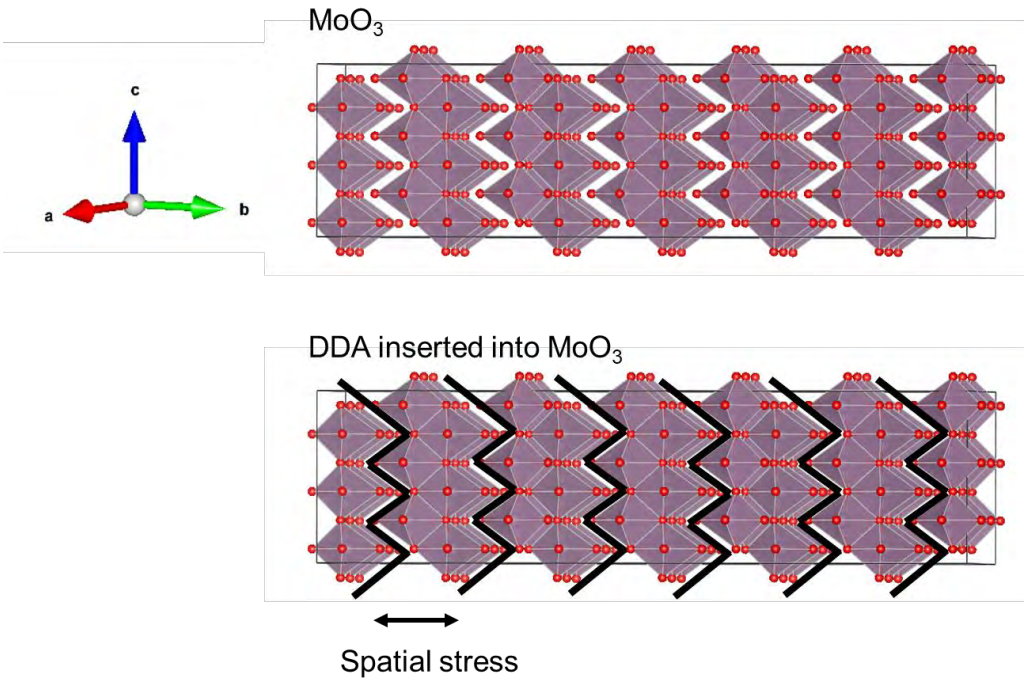

Figure S4. MoO_3 lattice (top) and DDA inserted into the MoO_3 lattice (bottom).

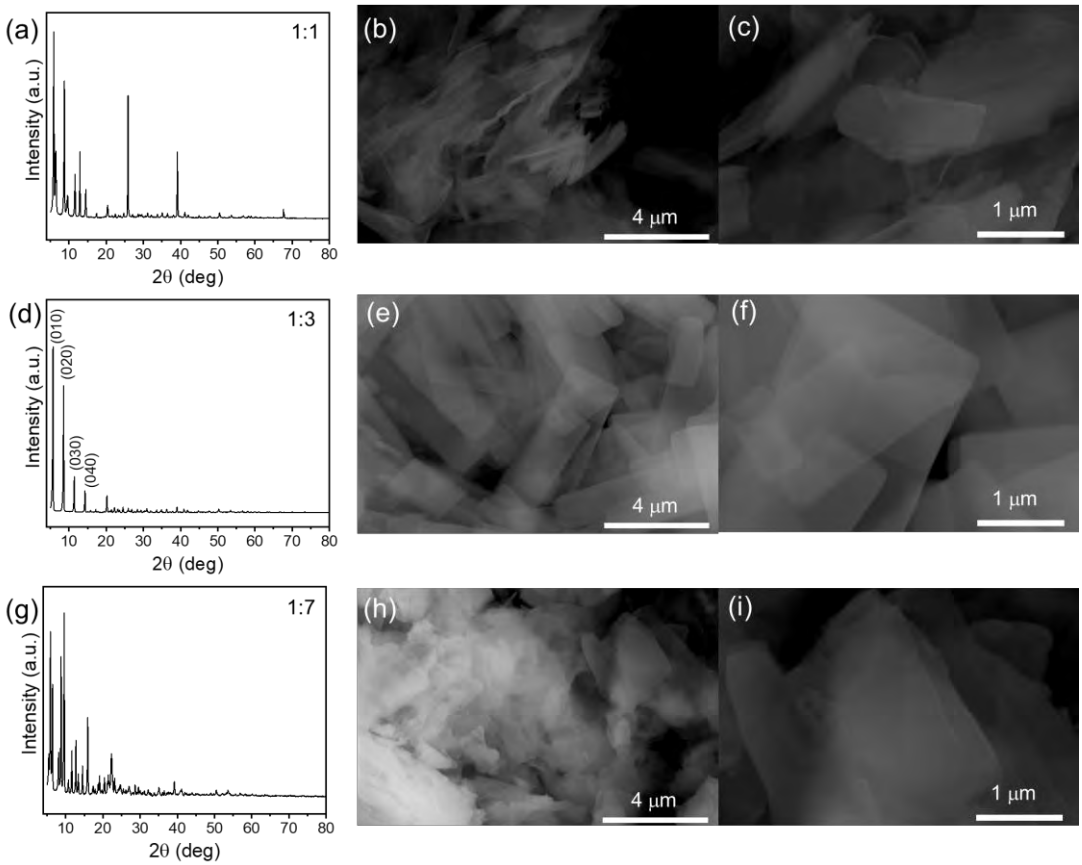

Figure S5. XRD patterns and SEM images of the samples with different molar ratios of MoO_3 to DDA: (a) 1:1, (d)–(f) 1:3, and (g)–(i) 1:7.

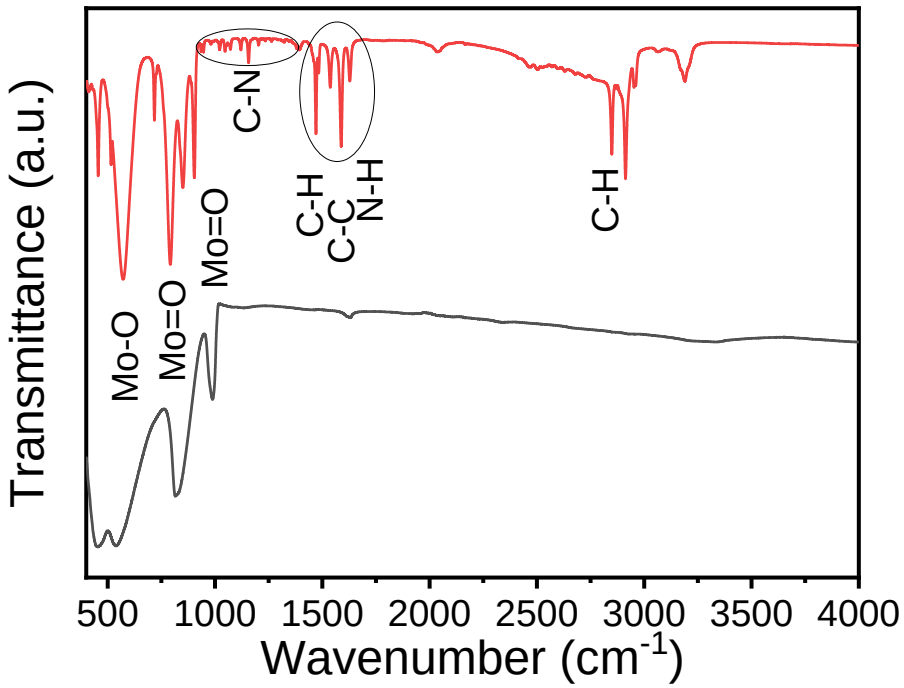

Figure S6. FTIR spectrum of MoN/NC.

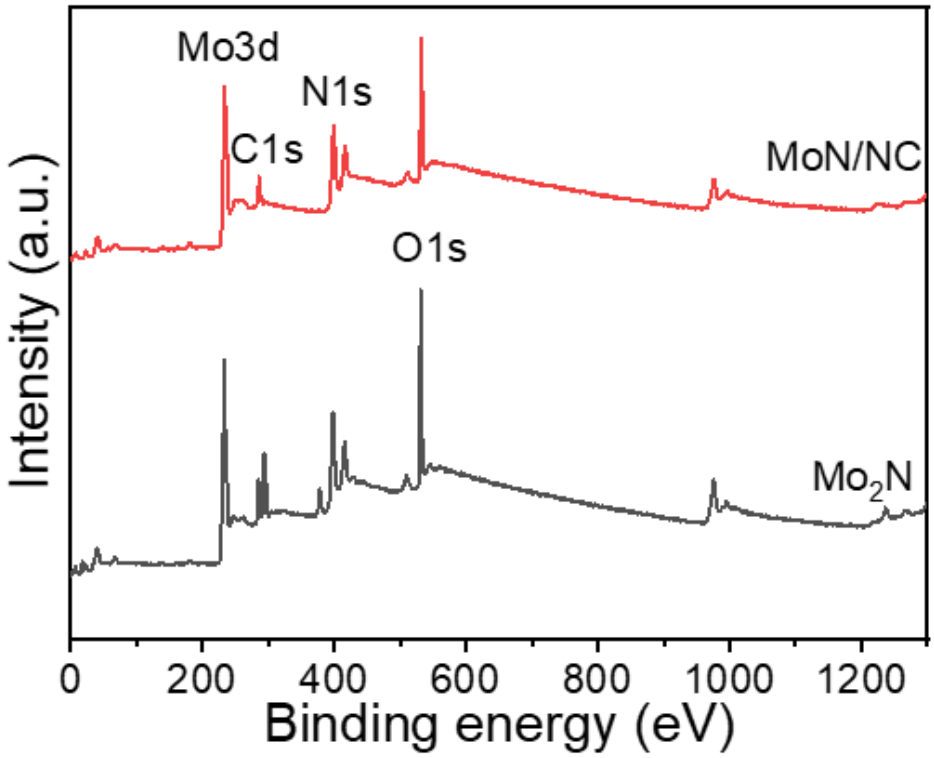

Figure S7. XPS spectra of MoN/NC and Mo_2N.

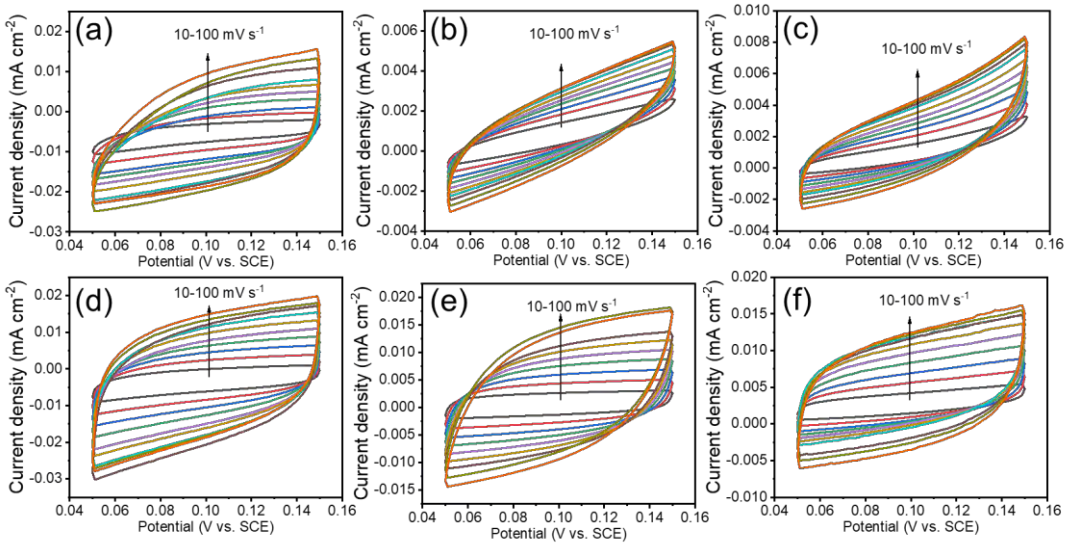

Figure S8. CV curves of MoN/NC in (a) 0.5 M H_2SO_4, (b) 1 M PBS, and (c) 1 M KOH; CV curves of Mo_2N in (d) 0.5 M H_2SO_4, (e) 1 M PBS, and (f) 1 M KOH.

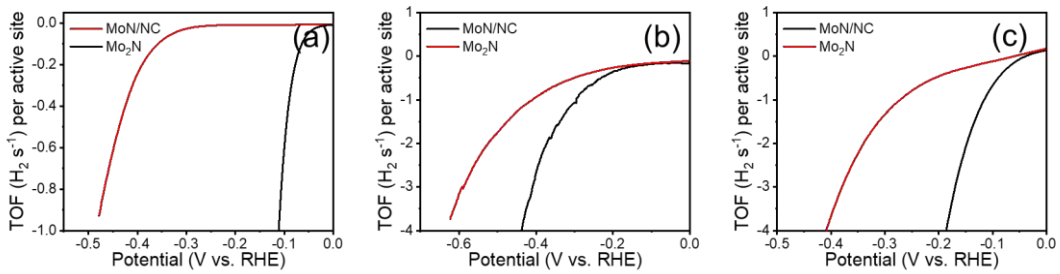

Figure S9. TOF of MoN/NC and Mo_2N in (a) 0.5 M H_2SO_4, (b) 1 M PBS, and (c) 1 M KOH.

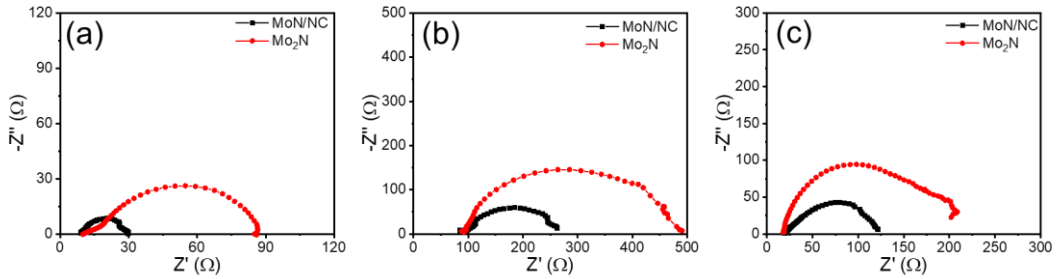

Figure S10. EIS curves of MoN/NC and Mo_2N in (a) 0.5 M H_2SO_4, (b) 1 M PBS, and (c) 1 M KOH.

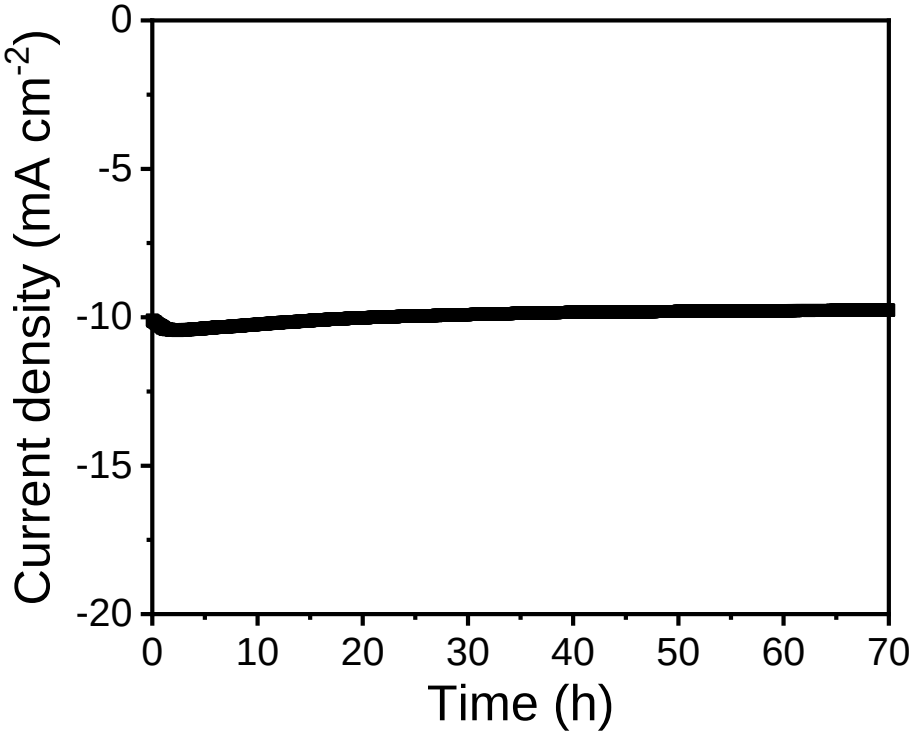

Figure S11. I-t curves of MoN/NC at the fixed overpotential of -0.1 V (versus SCE).

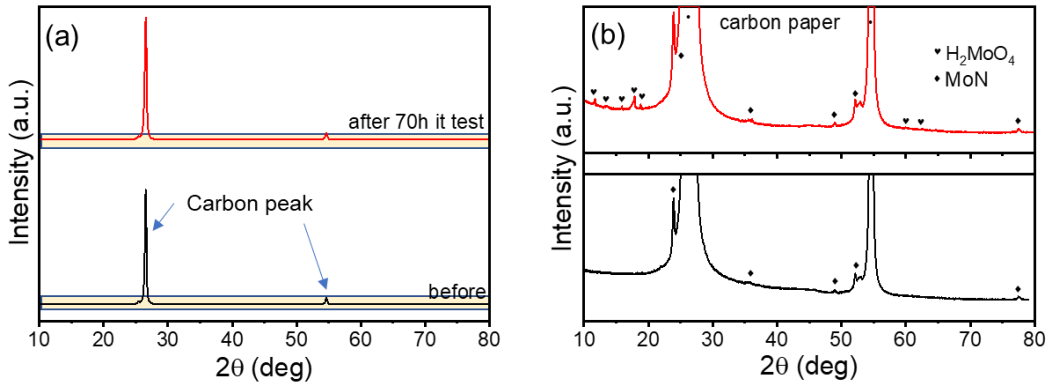

Figure S12. (a) XRD spectra of MoN/NC on carbon cloth before and after the i-t test for 70 h at the fixed overpotential of -0.1 V and (b) Magnified region in (a).

Table S1. Comparison of the properties of Mo_xN-based catalysts for HER.

Electrodes	media	Overpotential (mV) (10 mA cm^{-2})	Tafel slope (mV dec^{-1})	References
MoN/NC	0.5M H_2SO_4	93	44.5	This work
MoN/NC	1 M PBS	211	83.2	This work
MoN/NC	1 M KOH	141	65.4	This work
MoS_2-Mo_2N/CC	0.5 M H_2SO_4	121	49.6	[3]
Dr-MoN-0	0.5 M H_2SO_4	125	51.5	[4]
MoN	1 M KOH	400	120.6	[5]
C_3N_4/MoN mixture	1 M KOH	270	90.5	[5]
Co-MoN	1 M KOH	132 (at 100 mV)	77.5	[6]
Ni/MoN@NF	1 M KOH	--	54.8	[7]
MoN@NF	1 M KOH	--	66.6	[8]
MoN_x	0.5 M H_2SO_4	200	114	[9]
MoN_x	0.1 M KOH	240	121	[9]
MoS_2/MoN	0.5 M H_2SO_4	117	87	[10]

References

[1] Liao Z. H., Li Q. W., Zhang J. B., Xu J., Gao B. A., Chu P. K. and Huo K. F., Oriented MoS2 Nanoflakes on N-Doped Carbon Nanosheets Derived from Dodecylamine-Intercalated MoO3 for High-Performance Lithium-Ion Battery Anodes, Chemelectrochem, 2018;5(10):1350-1356.
[2] Qiu J. Y. C., Yang Z. X. and Li Y., N-doped carbon encapsulated ultrathin MoO3 nanosheets as superior anodes with high capacity and excellent rate capability for Li-ion batteries, Journal of Materials Chemistry A, 2015;3(48):24245-24253.
[3] Huang C., Ruan Q., Song H., Luo Y., Bai H., Gao B. and Chu P. K., Vertical kinetically oriented MoS_2–Mo_2N heterostructures on carbon cloth: a highly efficient hydrogen evolution electrocatalyst, Sustainable Energy & Fuels, 2020;4(5): 2201:2201-2207.
[4] Xiong J., Cai W. W., Shi W. J., Zhang X. L., Li J., Yang Z. H., Feng L. G. and Cheng H. S., Salt-templated synthesis of defect-rich MoN nanosheets for boosted hydrogen evolution reaction, Journal of Materials Chemistry A, 2017;5(46):24193-24198.
[5] Jin H. Y., Liu X., Jiao Y., Vasileff A., Zheng Y. and Qiao S. Z., Constructing tunable dual active sites on two-dimensional C_3N_4@MoN hybrid for electrocatalytic hydrogen evolution, Nano Energy, 2018;53:690-697.
[6] Sun J. W., Xu W. J., Lv C. X., Zhang L. J., Shakouri M. S., Peng Y. H., Wang Q. Q., Yang X. F., Yuan D., Huang M. H., Hu Y. F., Yang D. J. and Zhang L. X., Co/MoN hetero-interface nanoflake array with enhanced water dissociation capability achieves the Pt-like hydrogen evolution catalytic performance, Applied Catalysis B-Environmental, 2021;286:119882.
[7] Sun J. H., Guo F. F., Li X. Y., Yang J. and Ma J. F., Constructing Ni/MoN heterostructure nanorod arrays anchored on Ni foam for efficient hydrogen evolution reaction under alkaline conditions, Sustainable Energy & Fuels, 2021;5(21):5565-5573.
[8] Shi Y., Zhou Y., Yang D.-R., Xu W.-X., Wang C., Wang F.-B., Xu J.-J., Xia X.-H. and Chen H.-Y., Energy level engineering of MoS_2 by transition-metal doping for accelerating hydrogen evolution reaction, Journal of the American Chemical Society, 2017;139(43):15479-15485.
[9] Ramesh R., Nandi D. K., Kim T. H., Cheon T., Oh J. and Kim S. H., Atomic-Layer-Deposited MoNx Thin Films on Three-Dimensional Ni Foam as Efficient Catalysts for the Electrochemical Hydrogen Evolution Reaction, Acs Applied Materials & Interfaces, 2019;11(19):17321-17332.
[10] Wu A. P., Gu Y., Xie Y., Yan H. J., Jiao Y. Q., Wang D. X. and Tian C. G., Interfacial engineering of MoS2/MoN heterostructures as efficient electrocatalyst for pH-universal hydrogen evolution reaction, Journal of Alloys and Compounds, 2021;867.